Interaction-induced chiral $p_x \pm ip_y$ superfluid order of bosons in an optical lattice

2013 New J. Phys. 15 083041

(http://iopscience.iop.org/1367-2630/15/8/083041)

New Journal of Physics
The open access journal for physics

Interaction-induced chiral $p_x \pm ip_y$ superfluid order of bosons in an optical lattice

M Ölschläger[1], T Kock[1], G Wirth[1], A Ewerbeck[1], C Morais Smith[2] and A Hemmerich[1,3]

[1] Institut für Laser-Physik, Universität Hamburg, Luruper Chaussee 149, D-22761 Hamburg, Germany
[2] Institute for Theoretical Physics, Utrecht University, Leuvenlaan 4, 3584-CE Utrecht, The Netherlands
E-mail: hemmerich@physnet.uni-hamburg.de

New Journal of Physics **15** (2013) 083041 (15pp)
Received 6 May 2013
Published 22 August 2013
Online at http://www.njp.org/
doi:10.1088/1367-2630/15/8/083041

Abstract. The study of superconductivity with unconventional order is complicated in condensed matter systems by their extensive complexity. Optical lattices with their exceptional precision and control allow one to emulate superfluidity avoiding many of the complications of condensed matter. A promising approach to realize unconventional superfluid order is to employ orbital degrees of freedom in higher Bloch bands. In recent work, indications were found that bosons condensed in the second band of an optical chequerboard lattice might exhibit $p_x \pm i\,p_y$ order. Here we present experiments, which provide strong evidence for the emergence of $p_x \pm i\,p_y$ order driven by the interaction in the local p-orbitals. We compare our observations with a multi-band Hubbard model and find excellent quantitative agreement.

[3] Author to whom any correspondence should be addressed.

Contents

1. Introduction

Understanding the role of unconventional order for superconductivity is a fundamental task in low temperature physics. Prominent examples in condensed matter are transition metal oxides [1]. Studying the order parameters in these systems is complicated by their vast complexity. A widely debated example is the chiral $p_x + ip_y$ order possibly formed in strontium ruthenates [2], which has recently attracted much interest because its topological nature may give rise to Majorana fermions [3]. Optical lattices in their lowest band have proven to be a useful experimental arena to emulate superfluidity with exceptional precision and control [4, 5]. However, since under most general circumstances bosonic ground state wavefunctions are necessarily positive definite [6, 7] and hence topologically trivial, the realization of unconventional superfluid order in optical lattices with bosons is not straight forward. Possible approaches, presently receiving great attention, are based upon amending the scalar light-shift potentials of conventional optical lattices by static abelian and even non-abelian artificial gauge fields [8–11] or upon use of dynamical lattice potentials [12–14]. A method, more closely geared to electronic matter, is to employ atoms in metastable higher bands which provide orbital degrees of freedom [15, 16]. Recently, we have shown that upon suitable control of band relaxation bosons can be condensed in the second band of a bipartite square lattice [17]. Momentum spectra were observed consistent with chiral $p_x \pm ip_y$ superfluid order characterized by a spontaneously formed pattern of staggered local angular momenta, which breaks time-reversal symmetry. In this work, by means of the following line of arguments we present clear evidence that $p_x \pm ip_y$ order is in fact formed. We show that for the lowest energy state of a bosonic Hubbard-model accounting for the second, third and fourth bands, the repulsive interaction in the p-orbitals stabilizes $p_x \pm ip_y$ order in analogy to Hund's second rule in multi-electronic atoms. We calculate a characteristic phase diagram with respect to a change of the interaction in the local p-orbitals and an adjustable distortion of the lattice, which tunes the energy minima of the second band. Experimental observations are presented, which show excellent quantitative agreement with the theoretical predictions of this phase diagram. We finally discuss excited state scenarios, which are compatible with the previously observed momentum spectra, but inconsistent with the experimental signatures reported in this work.

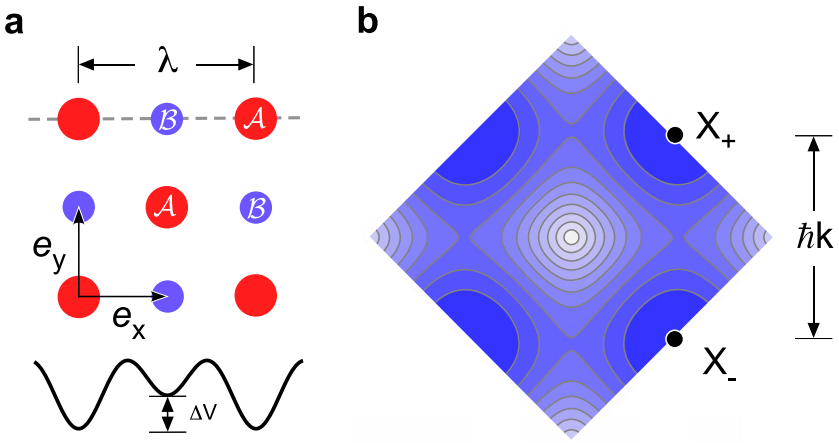

Figure 1. (a) The lattice possesses deep ($\mathcal{A}$) and shallow ($\mathcal{B}$) wells. λ denotes the laser wavelength. A section of the potential along the dashed gray line is shown at the lower edge with the tunable relative potential energy offset ΔV indicated. (b) Contour plot of the second band within the first Brillouin zone for $V_0 = 6E_{\mathrm{rec}}$, $\Delta V = 5.7E_{\mathrm{rec}}$. High and low energies are indicated by light gray and dark blue, respectively. The band exhibits two inequivalent local minima denoted as $X_\pm = \frac{1}{2}\hbar k\,(1, \pm 1)$ ($k = \lambda/2\pi$) at the edge of the first Brillouin zone.

2. Lattice potential

We produce a two-dimensional optical potential comprising deep and shallow wells ($\mathcal{A}$ and $\mathcal{B}$ in figure 1(a)) arranged as the black and white fields of a chequerboard with an average well depth V_0 and an adjustable relative potential energy offset ΔV [17–19]. In the xy-plane the optical potential is given by

$$V(x, y) \equiv -\frac{V_0}{4}\left|\eta\left(\mathrm{e}^{\mathrm{i}kx} + \epsilon_x\,\mathrm{e}^{-\mathrm{i}kx}\right) + \mathrm{e}^{\mathrm{i}\beta}\left(\mathrm{e}^{\mathrm{i}ky} + \epsilon_y\,\mathrm{e}^{-\mathrm{i}ky}\right)\right|^2 . \tag{1}$$

Adjustment of β permits controlled tuning of $\Delta V \equiv V_0\,\eta(1+\epsilon_x)(1+\epsilon_y)\cos(\beta)$. A weak harmonic potential along the z-direction provides elongated tubular lattice sites. If $\eta = \epsilon_x = \epsilon_y = 1$, the lattice potential possesses perfect C_4 rotation symmetry. In our experiment, we are constrained to fixed parameter values $\eta = 1.03$ and $\epsilon_x = 0.93$, and hence C_4 symmetry is weakly broken. In contrast to [17], careful power and polarization management of the lattice beams permits controlled adjustment of arbitrary values of ϵ_y around unity. The second Bloch band, shown in figure 1(b), provides two inequivalent local minima at the edge of the first Brillouin zone (denoted by X_+ and X_-), which are energetically degenerate if the lattice displays C_4 rotation symmetry. By adjusting the lattice distortion parameter ϵ_y (see the appendix), we can continuously tune their energy difference $\Delta E \equiv E(X_-) - E(X_+) \sim 1 - \epsilon_y$. In a tight-binding (TB) picture, the quantum states corresponding to $X_\pm$ may be approximated by Bloch states $|\psi_\pm\rangle$ with real-valued Bloch functions $\psi_\pm(r)$ composed of local p-orbitals (p_x, p_y) in the deep wells and local s-orbitals in the shallow wells. Denoting their occupations per unit cell as n_p and n_s with $n_0 \equiv n_\mathrm{s} + n_\mathrm{p}$, the relative occupations $\nu_\mathrm{p} \equiv n_\mathrm{p}/n_0$ and $\nu_\mathrm{s} \equiv n_\mathrm{s}/n_0$ only depend on the spatial shape of $\psi_\pm(r)$ (but not on the local chemical potential) and hence can be tuned via adjustment of ΔV (see the appendix).

3. Multi-band Hubbard model

In order to predict the nature of the expected quantum phases for different values of n_p and ΔE, we employ a bosonic multi-band Hubbard–Hamiltonian $\hat{H}$ (see the appendix) accounting for the three TB bands associated with the three local orbitals p_x, p_y and s. We include nearest-neighbor (NN) and next-NN (NNN) tunneling processes, on-site interactions for the p- and s-orbitals (as is indicated in figure A.1(f) of the appendix), and a term accounting for a potential energy difference between p- and s-orbitals, required for modeling the tuning of ΔV. Furthermore, an extra term is included, which introduces a quadrupolar anisotropy of the tunneling between p-orbitals with respect to the $(e_x + \mu e_y)$-directions (with $e_{x,y}$ shown in figure 1(a) and $\mu \in \{-1, 1\}$). This term with the real amplitude $J_{\parallel,a}$ permits to model the tuning of ΔE according to the relation $\Delta E \approx 8\nu_\mathrm{p} J_{\parallel,a}$, which is obtained by evaluating the single-particle spectrum of $\hat{H}$ in momentum space at $X_\pm$. Comparing the lowest two TB bands of $\hat{H}$ with the second and third bands of a full two-dimensional band calculation for the experimentally realized lattice potential lets us determine the tunneling parameters. The largest tunneling amplitude J_sp arises for NN-tunneling between s- and p-orbitals (see the appendix).

For $\Delta E = 0$, any linear combination $|\theta, \phi\rangle \equiv \sin(\theta)\,|\psi_+\rangle + \cos(\theta)\,\mathrm{e}^{\mathrm{i}\phi}|\psi_-\rangle$ minimizes the single-particle energy. For repulsive collisions, minimization of the interaction energy in the p-orbitals requires maximal angular momentum [15, 16] and hence $\phi = \pm\pi/2$ and $\theta = \pi/4$ because the local superposition states $\mathrm{p}_x \pm \mathrm{i}\mathrm{p}_y$ are maximally delocalized such that the atoms can optimally avoid each other. For $\Delta E \neq 0$, depending on the sign of ΔE, either $|\psi_+\rangle$ or $|\psi_-\rangle$ minimizes the single-particle energy. When ΔE is increased beyond some critical value, the gain of single particle energy exceeds the cost of interaction energy required for eliminating angular momentum, and hence also the total energy is minimized by one of the states $|\psi_\pm\rangle$. A mean field analysis for the general case $\Delta E \neq 0$ shows that the ground state of $\hat{H}$ can be in fact approximated as $|\theta, \pm\pi/2\rangle = \sin(\theta)\,|\psi_+\rangle \pm \mathrm{i}\cos(\theta)\,|\psi_-\rangle$ with the mixing angle θ plotted in the phase diagram in the center of figure 2 versus $J_{\parallel,a}$ and $n_\mathrm{p}U_\mathrm{p}$ (U_p is the on-site collision energy per particle in the p_x- and p_y-orbitals). Note that $\sin^2(\theta)$ and $\cos^2(\theta)$ quantify the relative populations of the condensation points X_+ and X_-, respectively. This phase diagram comprises three regions, separated by second-order phase boundaries highlighted by white dashed lines. In regions (I) and (III) one finds $\theta = 0$ and $\pi/2$ respectively (hence, only one of the condensation points $X_\pm$ in figure 1(b) is occupied), while in region (II) the simple relation

$$\cos(2\theta) = -\frac{12\,J_{\parallel,a}}{n_\mathrm{p}U_\mathrm{p}} = -\frac{3\,n_0\,\Delta E}{2\,n_\mathrm{p}^2\,U_\mathrm{p}} \tag{2}$$

holds[4]. The mixing of the two condensates is governed by a competition between the gain of single-particle energy per unit cell $n_0\,\Delta E$ introduced by the lattice distortion and the interaction energy per unit cell $n_\mathrm{p}^2\,U_\mathrm{p}$ gained by maximizing angular momentum in the p-orbitals. The pictograms on the upper edge of the phase diagram illustrate the orbital and local phase ordering predicted in the three regions. In regions (I) and (III) the order parameters are real and their local phases indicated by the colors and numbers are arranged in order to maximize tunneling, while interaction energy does not play a role. In region (II) an inherently complex-valued order arises with orbital currents and plaquette currents highlighted by circular and straight arrows,

[4] The first equality has been derived with contributions by O Tieleman.

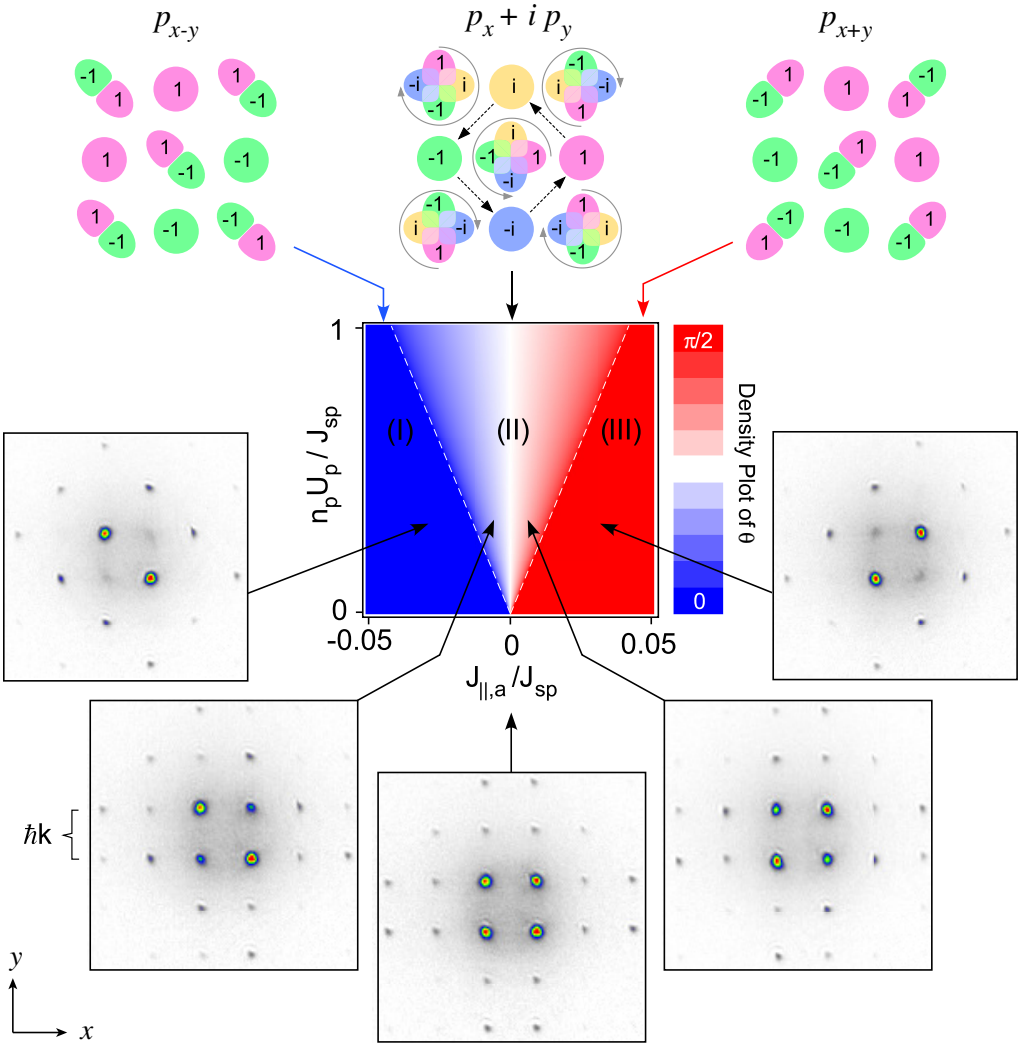

Figure 2. The phase diagram in the center shows the mixing angle θ versus $n_p U_p$ and $J_{\|,a}$ (in units of J_{sp}). Three phases arise (regions (I)–(III)) separated by second order transitions (white dashed lines). On the upper edge the corresponding orbital and phase ordering is illustrated. Orbital currents and plaquette currents are highlighted by circular and straight arrows. The colors and numbers indicate the local phases of the different local orbitals. Below the phase diagram momentum spectra are shown for different values of $J_{\|,a}$.

respectively. Interaction energy sets the relative local phases between p_x- and p_y-orbitals at the same site to be $\pi/2$, while the phase relations between orbitals at neighboring sites are arranged to maximize tunneling. The unit cell of the order parameter comprises four unit cells of the lattice potential and time-reversal is equivalent to a shift by one unit cell of the lattice potential. Hence, time-reversal symmetry is broken. Our theoretical considerations are consistent with a numerical analysis based upon the Gross–Pitaevskii equation [20] and a renormalization group analysis [21].

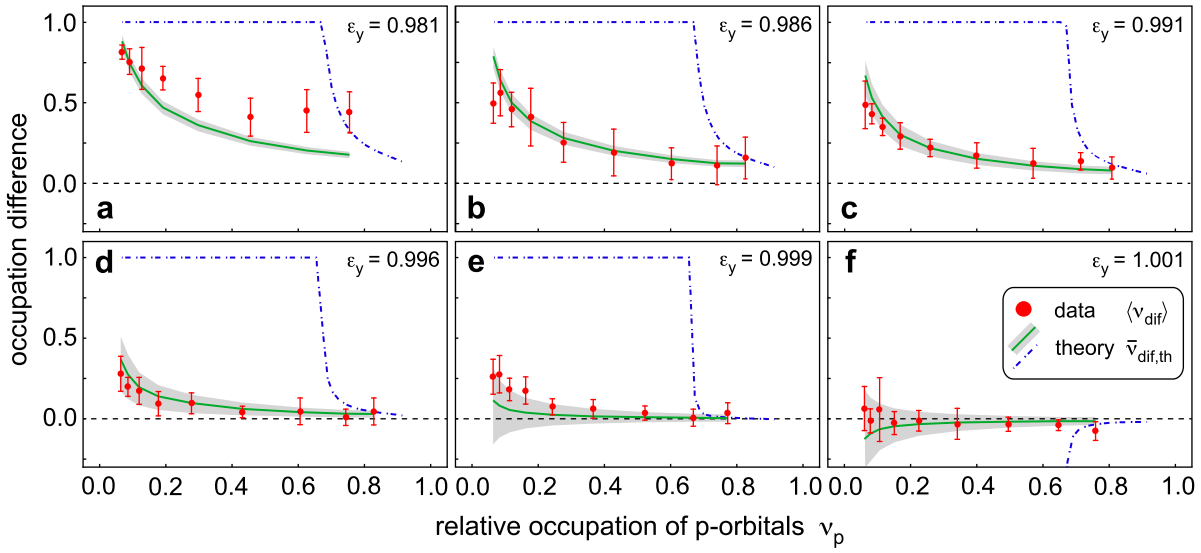

Figure 3. The normalized mean occupation difference $\langle\nu_{\mathrm{dif}}\rangle$ between the two condensation points $X_\pm$ is plotted versus the relative occupation of the p-orbitals ν_{p}. The error bars show the statistical errors for eight measurements. The adjusted distortion of the lattice potential is $1-\epsilon_y = 0.019$, 0.014, 0.009, 0.004, 0.001, -0.001 from (a) to (f). The solid green lines show the corresponding theoretical predictions $\bar{\nu}_{\mathrm{dif,th}}$ derived by means of equation (2). The gray areas represent the uncertainty of the lattice distortion $\Delta\epsilon_y = \pm 2.5 \times 10^{-3}$. The blue dashed lines show the predictions for scenario D.

4. Experiment

Our experimental procedure begins with a Bose–Einstein condensate of rubidium atoms (^{87}Rb) loaded into the lowest band. By means described in [17] the atoms are excited to the second band. Their temperature remains sufficiently low, such that after typically 10 ms they condense in the energy minima of the band. In our experiments we wait for 80 ms to ensure complete thermalization. Below the phase diagram in figure 2, we show momentum spectra observed in the different areas (I)–(III). In regions (I) and (III) the observed Bragg-resonances unambiguously prove the realization of the predicted standing-wave order in configuration space sketched in the corresponding pictograms. In region (II), where both points X_+ and X_- are populated, the momentum spectra appear as superpositions of those in regions (I) and (III). This clearly confirms that the underlying quantum state is composed of two states $|\psi_\pm\rangle$ corresponding to condensates at $X_\pm$ with $\mathrm{p}_{x\pm y}$ order. However, a more precise determination of its nature requires additional information. In the following, we show that the state prepared in our experiment closely follows the phase diagram in figure 2 derived for the ground state $|\theta, \pm\pi/2\rangle$ of $\hat{H}$, which we refer to as scenario A.

In figure 3 we compare the observed populations of the condensation points $X_\pm$ as a function of ν_{p} and the lattice distortion with the predictions of scenario A. The experimental procedure yielding the data points (filled red discs) in figures 3(a)–(f) is as follows. For different settings of the lattice distortion parameter ϵ_y, ΔV is varied adiabatically and the normalized mean occupation difference between both condensation points $\langle\nu_{\mathrm{dif}}\rangle \equiv (\langle n_+\rangle - \langle n_-\rangle)/(\langle n_+\rangle + \langle n_-\rangle)$ is recorded and plotted versus ν_{p}. Here, $n_\pm$ are the populations observed in $X_\pm$

in a single measurement and $\langle \ldots \rangle$ denotes the average over multiple experimental realizations. For the small interaction energies realized in our system—with $U_\mathrm{p}/J_\mathrm{sp}$ on the order of a few per cent—and temperatures well below the condensation temperature, our mean field zero temperature analysis appears well adapted to model the observations if the finite size of the lattice with spatially varying local values of n_p and U_p is accounted for. In fact, upon applying a local density approximation, the observations are remarkably well reproduced by the theoretical predictions for scenario A. Using θ according to equation (2) with the local values of ΔE, n_p and U_p, we calculate the corresponding local value of $\nu_\mathrm{dif,th} \equiv \sin^2(\theta) - \cos^2(\theta)$ at each plaquette in the lattice and subsequently apply an average over all plaquettes to obtain $\overline{\nu}_\mathrm{dif,th}$, which is plotted as the solid green lines in figures 3(a)–(f). The gray areas reflect the largest uncertainty in this calculation given by the calibration of the lattice distortion parameter. A discussion of the technical details is given in the appendix. According to the observations in figure 3, n_+ and n_- approach each other if the distortion is reduced or if ν_p is increased, in excellent quantitative agreement with the predictions for region (II) of the phase diagram in figure 2, where the value of $J_{\parallel,a}$ and hence ΔE required to produce imbalanced condensate fractions grows with increasing ν_p. This striking behavior is hence identified as a signature of $\mathrm{p}_y \pm \mathrm{ip}_y$-order described by scenario A. The physical mechanism may be regarded as an analogue of Hund's second rule for repulsively interacting bosons: maximal local angular momentum is favorable in order to minimize interaction energy.

Aside from the ground state scenario A, the distribution of the Bragg-resonances in region (II) is also compatible with three possible excited-state scenarios: the coexistence of spatially separated real phases $|\psi_\pm\rangle$ (scenario B), a *real* coherent superposition $|\theta, (1 \mp 1)\pi/2\rangle \equiv \sin(\theta)\,|\psi_+\rangle \pm \cos(\theta)\,|\psi_-\rangle$ with $\mathrm{p}_{x+y} \pm \mathrm{p}_{x-y}$ order (scenario C), and an *incoherent mixture* described by the density operator $\rho_\theta \equiv \sin^2(\theta)\,|\psi_+\rangle\langle\psi_+| + \cos^2(\theta)\,|\psi_-\rangle\langle\psi_-|$ (scenario D). The compelling quantitative agreement of our observations with the predictions for the ground state scenario A is underlined by the fact that the excited state scenarios B–D lead to predictions in explicit contrast to the observations. The phase separation scenario B exhibits spatially separate p_{x+y} and p_{x-y}-orbitals corresponding to the two condensates $|\psi_\pm\rangle$. Hence, interaction energy does not favor equal populations of the condensation points and thus $\nu_\mathrm{dif,th}$ cannot acquire any dependence upon ν_p, in sharp contrast to the observations. The absence of phase separation in our experiment is also supported by the fact that in our Bragg spectra we never observe different coherence areas for the Bragg peaks corresponding to the two condensation points. This would be expected, if the measured condensate populations n_+ and n_- would be attributed to spatially separated $|\psi_\pm\rangle$-domains of different size. The irrelevance of scenario B in our experiments is not surprising. Coexisting spatially separated domains of real phases $|\psi_+\rangle$ and $|\psi_-\rangle$ as in scenario B are energetically more costly than either of the pure phases $|\psi_\pm\rangle$. A change of the domain sizes merely requires a local redistribution of particles between the p_{x+y} and p_{x-y}-orbitals. Particle transport over many lattice sites is not necessary. Hence, equilibration should occur within a few tunneling times leading to the formation of either $|\psi_+\rangle$ or $|\psi_-\rangle$. The real superposition state of scenario C exhibits spatially separate p_x and p_y-orbitals. For equal populations of the condensation points every second local s-orbital remains unoccupied due to destructive interference, which is energetically strongly unfavorable. In fact, minimization of the energy of $|\theta, (1 \mp 1)\pi/2\rangle$ with respect to θ yields either of the values $\theta = 0$ or $\pi/2$ only depending on the sign of ΔE and hence $\nu_\mathrm{dif,th}$ can only take the values ± 1 (see section A.10 of the appendix). Finally, although the incoherent mixture ρ_θ in scenario D provides orthogonal $\mathrm{p}_{x\pm y}$-orbitals at the same lattice site, the interaction energy

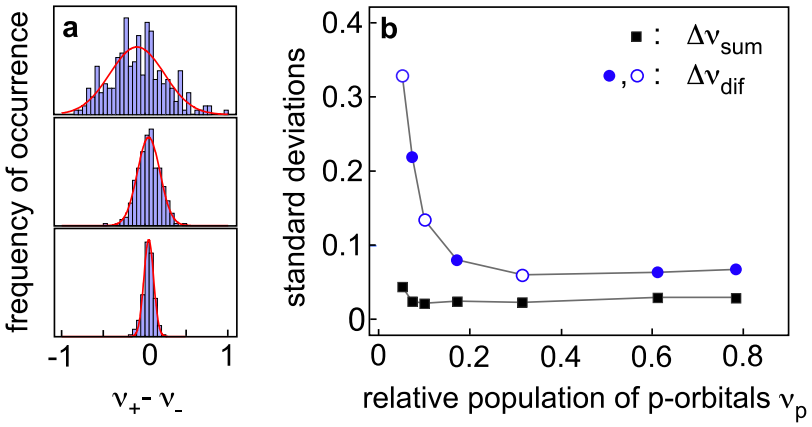

Figure 4. (a) Histograms of $\nu_+ - \nu_-$ for $\nu_p = 0.06$, 0.10 and 0.32 each showing more than 150 identical realizations. The red solid traces show Gaussian fits. (b) The standard deviations $\Delta\nu_{sum}$ and $\Delta\nu_{dif}$ are plotted versus ν_p (open and filled blue discs: $\Delta\nu_{dif}$, black squares: $\Delta\nu_{sum}$; the open discs correspond to the histograms shown in (a); the thin gray lines connecting the data points are for guiding the eye).

gained by equally distributing the atoms among these orbitals is smaller than for scenario A because of the indeterminate phase relation between the two states $|\psi_\pm\rangle$. We have minimized the energy of ρ_θ with respect to θ in order to determine $\overline{\nu}_{dif,th}$ for this scenario. The result (see the appendix, equation (A.3)) is plotted as the dashed blue lines in figure 3, which obviously disagrees with the observations. In fact, significantly larger values of ν_p would be required to equilibrate the condensate fractions as compared to scenario A. Scenario D also appears implausible because the two incoherently superimposed condensates can exchange particles through binary collisions in the shared local s-orbitals of the shallow wells (see pictograms of regions (I) and (III)). This should rapidly degrade the coherence in each condensate, which is not observed.

Further insight is gained by analyzing the fluctuations of $\nu_\pm \equiv n_\pm/\langle n_+ + n_-\rangle$. Histograms recorded for $\Delta E \approx 0$ show fluctuations of $\nu_+ - \nu_-$, well described by Gaussians, centered at $\nu_+ = \nu_-$ (see figure 4(a)). This observation appears incompatible with the phase separation scenario B, for which, similarly as in [14], a double peak structure should be expected instead, since equal populations $n_\pm$ of the two involved condensation points are not preferred. In figure 4(b) the standard deviations $\Delta\nu_{sum} \equiv (\langle(\nu_+ + \nu_-)^2\rangle - \langle\nu_+ + \nu_-\rangle^2)^{1/2}$ and $\Delta\nu_{dif} \equiv (\langle(\nu_+ - \nu_-)^2\rangle - \langle\nu_+ - \nu_-\rangle^2)^{1/2}$ are plotted versus ν_p. The observations show that $\langle\nu_+\nu_-\rangle - \langle\nu_+\rangle\langle\nu_-\rangle = (\Delta\nu_{sum}^2 - \Delta\nu_{dif}^2)/4$ significantly deviates from zero, i.e. the fluctuations of $\nu_\pm$ are strongly correlated. While the comparably small fluctuations of the total condensate fraction $\Delta\nu_{sum}$ show basically no dependence on ν_p, $\Delta\nu_{dif}$ is sizable and notably decreases as ν_p is increased, showing that the interaction in the p-orbitals tend to lock the populations condensed in X_+ and X_-. This observation again clearly rules out scenarios B and C, which do not prefer equal values of $n_\pm$ as ν_p is increased. It clearly reflects the physics of scenario A captured in the phase diagram in figure 2. As ν_p is decreased, the critical point is approached along the vertical $J_{\parallel,a} = 0$-line where all three phases adjoin. The larger ν_p the higher the interaction energy to be paid for deviations of $\nu_+ - \nu_-$ from zero yielding suppression of fluctuations $\Delta\nu_{dif}$.

5. Conclusion

Optical lattices with $p_x \pm ip_y$ order open exciting perspectives for future research. Matter wave interference techniques [22] could be used to further study the mutual coherence of the condensates at X_+ and X_-. Imaging of the atoms with single-site resolution as demonstrated in [23, 24] might allow one to directly observe the local angular momentum of the wave function and hence to explore the spontaneous symmetry breaking process. Proceeding to deeper potential wells, one may access the strongly correlated regime where a rich phase diagram of Mott insulators with distinct orbital ordering is expected [25–27]. One may also explore topologically protected features in higher bands [28] and, if fermions are used, simulate forms of topological matter [29] resembling those discussed in the context of electronic systems.

Acknowledgments

This work was partially supported by DFG-He2334/14-1, DFG-SFB 925, DFG-GrK1355 and the Netherlands Organization for Scientific Research (NWO). We are grateful to L Mathey and W Vincent Liu for useful discussions.

Appendix

A.1. Lattice potential

Using an interferometric lattice set-up [18], we produce a two-dimensional optical potential comprising deep and shallow wells ($\mathcal{A}$ and $\mathcal{B}$ in figure 1(a) of the main text) arranged as the black and white fields of a chequerboard with an average well depth V_0 and an adjustable relative potential energy offset [17]. In the xy-plane the optical potential is given by

$$V(x, y) \equiv -\frac{V_0}{4} \left| \eta \left(e^{ikx} + \epsilon_x e^{-ikx}\right) + e^{i\beta} \left(e^{iky} + \epsilon_y e^{-iky}\right) \right|^2 . \tag{A.1}$$

Adjustment of β with a precision exceeding $\pi/300$ permits controlled tuning of $\Delta V \equiv V_0 \eta(1+\epsilon_x)(1+\epsilon_y)\cos(\beta)$. A weak harmonic potential (with 40 Hz vibrational frequency) along the z-direction provides elongated tubular lattice sites. If $\eta = \epsilon_x = \epsilon_y = 1$, the lattice potential possesses perfect C_4 rotation symmetry. In our experiment, due to unavoidable imperfections of the lattice set-up, we are constrained to fixed parameter values $\eta = 1.03$, and $\epsilon_x = 0.93$ and hence C_4 symmetry is weakly broken. In contrast to [17], the optical set-up permits controlled adjustment of arbitrary values of ϵ_y within an interval including $\epsilon_y = 1$. This is accomplished as follows: the optical standing wave along the y-axis is obtained by a retro-reflected laser beam. The linear polarization of the incoming beam can be rotated with a retardation plate. After retro-reflection the polarization is rotated to precisely match with the z-direction, which exclusively contributes to the lattice potential.

A.2. Band structure: tight-binding picture and full-band calculation

One may understand the single-particle bands within a simplified TB picture. As sketched in figure A.1(a), each local vibrational orbital of the two types of wells gives rise to a Bloch band. We operate in the regime where the second, third and fourth bands are significantly closer to each other than their separation from the first band, which correspond to the local

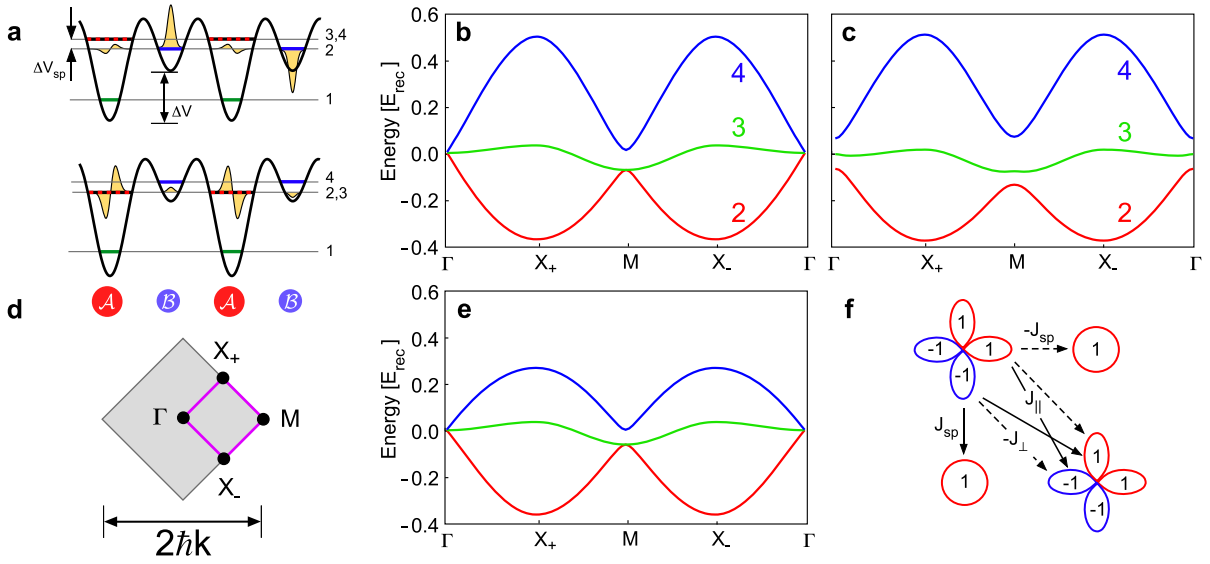

Figure A.1. (a) Schematic of first four bands plotted in configuration space for $\Delta V_{\rm sp} < 0$ (upper detail) and $\Delta V_{\rm sp} > 0$ (lower detail). The black and red dashed lines represent degenerate local p_x- and p_y-orbitals yielding two closely spaced bands. In (b) and (c) the second (red), third (green) and fourth (blue) Bloch bands are plotted along a roundtrip in the first Brillouin zone (gray square in (d)) connecting the points Γ, X_+, M, X_-, Γ. Panels (b) and (c) show the idealized C_4-symmetric case ($\eta = \epsilon_x = \epsilon_y = 1$) and the experimentally implemented case ($\eta = 1.03$, $\epsilon_x = 0.93$, $\epsilon_y = 1$), respectively. (e) TB bands based upon the Hamiltonian in equation (A.2) fitted to match the bands in (b). (f) Tunneling amplitudes used in the Hubbard model in equation (A.2). The numbers ν plotted inside the local s- and p-orbitals denote their local phases $e^{i(\nu-1)\pi/2}$.

s-ground states in the deep wells. We may write $\Delta V = V_{\rm sp} + \Delta V_{\rm sp}$ with a potential energy offset $V_{\rm sp}$ depending on the adjusted value of V_0, and $\Delta V_{\rm sp}$ denoting the potential energy difference between the local s-states in the shallow wells and the local p_x and p_y orbitals in the deep wells (cf figure A.1(a)). For $V_0 = 6E_{\rm rec}$ used in our experiment, $V_{\rm sp} = 5.7E_{\rm rec}$. If $\Delta V_{\rm sp} < 0$, the second band arises primarily from the local s-states in the shallow wells (upper graph in figure A.1 (a)), while for $\Delta V_{\rm sp} > 0$ it corresponds to a superposition of the degenerate p_x- and p_y-orbitals in the deep wells (lower graph in figure A.1 (a)). A two-dimensional band calculation for the potential in equation (A.1) yields the true second, third and fourth Bloch bands. In figures A.1(b) and (c), these bands are plotted along a roundtrip in the first Brillouin zone connecting the points Γ, X_+, M, X_-, Γ (indicated in (d)). The average well depth is $V_0 = 6E_{\rm rec}$ and $\Delta V = 5.7E_{\rm rec}$, which corresponds to $\Delta V_{\rm sp} \approx 0$ in the TB picture in (a). In (b) the idealized C_4 symmetric case is shown, compared in (c) to the experimentally implemented case with $\epsilon_y = 1$. The band degeneracies arising at the Γ- and M-points in (b) are lifted in (c) due to the lattice distortion. In either case the second band possesses two inequivalent band minima at the X_-- and X_+-points with energies $E(X_\pm)$, which are degenerate even in the case (c) despite the broken C_4-symmetry. Only if ϵ_y is tuned away from unity, this degeneracy is lifted. Experimentally, tuning of $\Delta E \equiv E(X_-) - E(X_+)$ is accomplished by tuning of ϵ_y with $\Delta E(\epsilon_y) \sim 1 - \epsilon_y$

quantified by a band calculation for the potential in equation (A.1). In the vicinity of the X_-- and X_+-points, where the condensed atoms reside, the bands in (b) and (c) are approximately equal.

A.3. Bosonic multi-band Hubbard model

We employ the multi-band Hubbard–Hamiltonian

$$\begin{aligned}\hat{H} \equiv & -J_{ss} \sum_{R\in\mathcal{B},\mu,\nu} \hat{s}_R^\dagger \hat{s}_{R+\mu d_\nu} - J_{\mathrm{sp}} \sum_{R\in\mathcal{A},\sigma,\mu} (\mu\, \hat{p}_{\sigma,R}^\dagger \hat{s}_{R+\mu e_\sigma} + \text{h.c.}) \\ & - \sum_{R\in\mathcal{A},\sigma,\mu,\nu} (J_\parallel + \nu J_{\parallel,a})\, \hat{p}_{\sigma,R}^\dagger\, \hat{p}_{\sigma,R+\mu d_\nu} - J_\perp \sum_{R\in\mathcal{A},\mu,\nu} \nu\, (\hat{p}_{x,R}^\dagger\, \hat{p}_{y,R+\mu d_\nu} + \hat{p}_{y,R}^\dagger\, \hat{p}_{x,R+\mu d_\nu}) \\ & + \frac{\Delta V_{\mathrm{sp}}}{2} \sum_{R\in\mathcal{A}} (\hat{n}_{\mathrm{s},R+e_x} - \hat{n}_{\mathrm{p},R}) + \frac{U_{\mathrm{p}}}{2} \sum_{R\in\mathcal{A}} (\hat{n}_{\mathrm{p},R}^2 - \hat{L}_{\mathrm{p},R}^2/3) + \frac{U_{\mathrm{s}}}{2} \sum_{R\in\mathcal{B}} \hat{n}_{\mathrm{s},R}(\hat{n}_{\mathrm{s},R} - 1)\end{aligned} \tag{A.2}$$

with the summation indices $\mu, \nu \in \{-1, 1\}$, $\sigma \in \{x, y\}$, $d_\nu \equiv e_x + \nu e_y$, and $e_{x,y}$ as shown in figure 1(a) of the main text. This Hamiltonian accounts for all possible tunneling processes between nearest-neighbors (NN) and next-NNs (NNN), as is indicated in figure A.1(f): NN-tunneling between s-orbitals and p-orbitals (J_{sp}), NNN-tunneling between s-orbitals (J_{ss}), NNN-tunneling between p_x-orbitals or p_y-orbitals ($J_\parallel$), NNN-tunneling between p_x- and p_y-orbitals ($J_\perp$), a term accounting for a potential energy difference between p- and s-orbitals (ΔV_{sp}) and the on-site interactions for p-orbitals (U_{p}) and s-orbitals (U_{s}), respectively, with $\hat{n}_{\mathrm{s},R} \equiv \hat{s}_R^\dagger \hat{s}_R$, $\hat{n}_{\mathrm{p},R} \equiv \hat{p}_{x,R}^\dagger\, \hat{p}_{x,R} + \hat{p}_{y,R}^\dagger\, \hat{p}_{y,R}$ and $\hat{L}_{\mathrm{p},R} \equiv \mathrm{i}(\hat{p}_{x,R}^\dagger\, \hat{p}_{y,R} - \hat{p}_{y,R}^\dagger\, \hat{p}_{x,R})$. Furthermore, an extra term scaling with $J_{\parallel,a}$ is included, which introduces a quadrupolar anisotropy of the tunneling between p-orbitals with respect to the d_ν-directions. This term permits to model the tuning of the energy difference ΔE between the minima of the second band. Diagonalizing the kinetic part of $\hat{H}$ in momentum space at $X_\pm$ yields the relation $\Delta E \approx 8\nu_{\mathrm{p}} J_{\parallel,a}$ with the relative occupation ν_{p} of the p-orbitals given as $\nu_{\mathrm{p}} \approx \frac{1}{2}[1 + \Delta V_{\mathrm{sp}}/(32J_{\mathrm{sp}}^2 + \Delta V_{\mathrm{sp}}^2)^{1/2}]$.

A.4. Determination of hopping parameters and phase diagram

The Hubbard Hamiltonian of equation (A.2) yields three TB bands associated with the three local orbitals involved. Setting $J_{\parallel,a} = 0$ we match the lowest two TB bands with the full bands in figure A.1(b). This lets us determine the tunneling parameters as $J_{\mathrm{ss}} \approx 0$, $J_{\mathrm{sp}} = 0.12E_{\mathrm{rec}}$, $J_\parallel = 0.07J_{\mathrm{sp}}$, $J_\perp = 0.15J_{\mathrm{sp}}$, and $\Delta V_{\mathrm{sp}} = 0.3J_{\mathrm{sp}}$. The resulting TB bands are plotted in figure A.1(e) showing good agreement with the full bands. The smaller bandwidth of the third TB band as compared to the corresponding fourth full band indicates the proximity of higher bands (p-orbitals in the shallow wells) in the true lattice potential, not accounted for in the TB-description. A non-zero value of $J_{\parallel,a}$ introduces an imbalance for NNN-tunneling between p-orbitals along the $x + y$ and $x - y$-directions, which acts to lift the degeneracy of the two band minima of the lowest TB band. The phase diagram in equation (1) of the main text is derived as follows. The Hamiltonian in equation (A.2) including $J_{\parallel,a}$ is rewritten, using a composition of the lattice via plaquettes with four sites. We diagonalize the kinetic energy in momentum

space and assume that the system is condensed at the two inequivalent energy minima of the lowest TB band. Replacing momentum space operators by their mean values, we calculate the interaction energy to zeroth order in the fluctuations and minimize the total energy with respect to the relative phase between the two possible condensation states and with respect to their relative weights.

A.5. Momentum spectra and band populations

Momentum spectra are obtained by rapidly ($<1\,\mu$s) extinguishing the lattice potential, permitting a free expansion of the atomic sample during 30 ms, and subsequently recording an absorption image. Band populations are measured as follows: the population of the nth band is transferred into the nth Brillouin zone by adiabatically terminating the lattice potential in 400 μ s, followed by a ballistic expansion of 30 ms. An absorption image of the atomic density distribution is recorded and the populations in the different Brillouin zones are counted.

A.6. Tuning of ν_p, effect of band relaxation

The required tuning of the relative population of the p-orbitals ν_p is accomplished via adjustment of ΔV. Since this tuning is essential, we have studied it in some detail. The value of ν_p corresponding to some β and ϵ_y (and hence ΔV and ΔE) is obtained by integrating $|\psi_\pm(r)|^2$ over those fields of the chequerboard lattice comprising the deep wells with the Bloch functions $\psi_\pm(r)$ at the condensation points $X_\pm$ derived from a band calculation employing the potential of equation (A.1). ν_p scales monotonously with ΔV (as shown by the solid black trace of figure A.2(a)) and it is practically independent of the lattice distortion parameter ϵ_y and hence of ΔE. This behavior is consistent with the approximate analytic expression derived from the Hubbard model in section A.3.

Changing ΔV also has a significant impact on the time-scale of band relaxation, as is shown by the data points in figure A.2(a). The band lifetime is found to be maximal (≈ 230 ms) if most atoms reside in the local s-orbitals ($\nu_p \approx 0$). This is expected, since for these atoms there is no local state with lower energy available, which could give rise to relaxation. The initial preparation of the condensate is carried out in this configuration. Following a holding time of 80 ms to reach complete equilibrium, a subsequent adiabatic increase of ν_p during 3 ms is directly visible in the momentum spectra: the higher order Bragg-peaks become more populated due to the increased contribution of the local p-orbitals, which due to their nodal structure comprise higher momenta. This is shown in figures A.2(b) and (c) with the corresponding calculation in figure A.2(d) yielding good agreement. Increasing values of ν_p are accompanied by faster band decay. Since a single tunneling process between adjacent wells is sufficient for adjusting ν_p, adiabaticity only requires tuning times of a few tunneling times of about 1 ms.

The lifetime of the atoms in the second band (figure A.2(a) red discs) is measured as follows: after forming the condensate at $\Delta V = 3E_{rec}$, ΔV is tuned in 3 ms (sufficiently slow to permit tunneling) to the desired value. After a variable duration the population of the second band is determined (see section A.5.). The wings of the decaying populations are fitted by exponentials with the $1/e$-times plotted as the red discs in figure A.2(a). The lifetimes of the condensed fraction (blue squares in figure A.2(a)) are obtained by an analogue procedure, however counting the number of atoms in the lowest order Bragg peaks of a momentum spectrum.

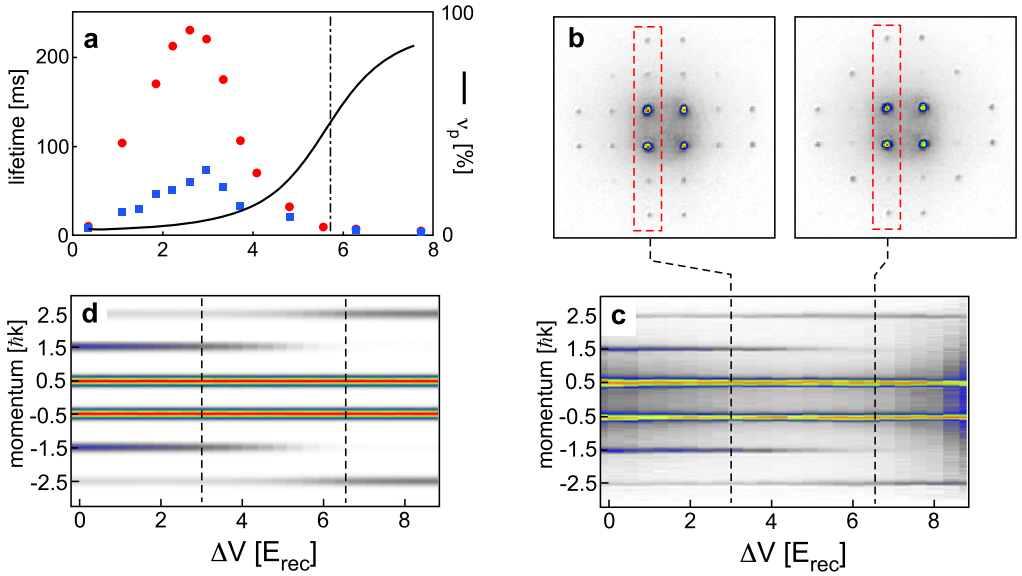

Figure A.2. (a) The data points show the lifetime of the atoms (red discs) and that of the condensed fraction (blue squares) in the second band versus ΔV for $V_0 = 6.0E_{\rm rec}$. The solid line (derived from a band calculation) shows the relative p-orbital population $\nu_{\rm p}$ versus ΔV. The vertical dashed-dotted line indicates $\Delta V = V_{\rm sp} = 5.7E_{\rm rec}$, where $\nu_{\rm p} = \nu_{\rm s} = 1/2$. (b) Two observations of momentum spectra recorded for small ($3.0E_{\rm rec}$) and large ΔV ($6.5E_{\rm rec}$). The red dashed rectangle identifies selected Bragg-maxima analyzed in more detail in (c) (observations) and (d) (theory) for varying values of ΔV.

A.7. Calibrating the lattice distortion ϵ_y

Changes of ΔE are experimentally implemented by adjustment of the lattice distortion parameter ϵ_y using polarization optics. Calibration of $\Delta E(\epsilon_y)$ proceeds as follows: the linear polarization of the incoming beam in the y-branch of the lattice potential is rotated such that $\langle n_+ \rangle \approx \langle n_- \rangle$, which corresponds to $\Delta E(\epsilon_y = 1) = 0$. Arbitrary values of ΔE are adjusted by rotating the polarization away from this position by precisely quantified amounts and determining the corresponding values of ΔE via a band calculation for the potential in equation (A.1). The estimated error in the determination of ϵ_y is $\Delta\epsilon_y \approx 2.5 \times 10^{-3}$.

A.8. Determination of $\overline{n_{\rm p}^2 U_{\rm p}}$, $\overline{n_0 \Delta E}$ and $\overline{\nu}_{\rm dif,th}$

We account for the isotropic harmonic potential with approximately 40 Hz trap frequency superimposed upon the two dimensional lattice of equation (A.1) with $\eta = \epsilon_x = \epsilon_y = 1$ and tubular lattice sites extending along the z-direction. The total number of condensed atoms, determined by fitting Gaussians to all visible Bragg peaks of a momentum spectrum and counting the atoms, is $N \approx 1.5 \times 10^4$ before band relaxation sets in. Assuming a Thomas–Fermi density distribution along the weakly confined z-direction, we calculate the local number of atoms per unit cell $n_{0,R}$ at the Bravais lattice site R, and hence the local number of particles in the s-orbitals and p-orbitals, $n_{{\rm s},R} = \nu_{\rm s}\, n_{0,R}$ and $n_{{\rm p},R} = \nu_{\rm p}\, n_{0,R}$, respectively. In the center

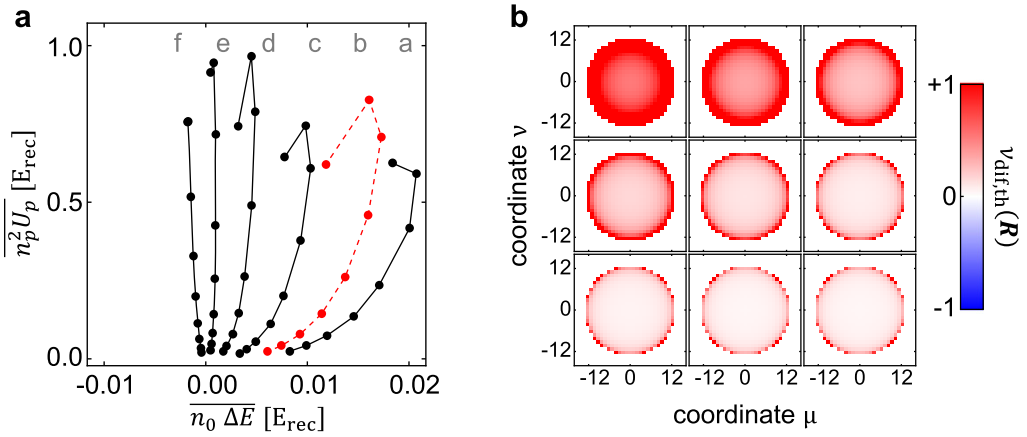

Figure A.3. (a) Map of the values of $\overline{n_p^2\,U_p}$ and $\overline{n_0\,\Delta E}$ for the data points in the graphs (a)–(f) in figure 3 of the main text. The kinks in the paths arise due to collisional losses setting in for large values of ν_p. (b) For the case of the red dashed path (b) corresponding to figure 3(b), the local value of $\nu_{dif,th}(R)$ is plotted across the lattice. The lattice is parameterized by the Bravais vectors $R = \mu\, d_+ + \nu\, d_-$.

of the lattice $n_{0,R} \approx 50$. In order to determine the local interaction energies per particle in the p-orbitals and s-orbitals at site R, $U_{p,R}$ and $U_{s,R}$, the local wells at the $\mathcal{A}$- and $\mathcal{B}$-sites are approximated to sixth order and the corresponding wave-functions of the local p-orbitals and s-orbitals are calculated. With this input, we determine the local energies $n_{p,R}^2\,U_{p,R}$ and $n_{0,R}\,\Delta E$. By applying equation (2) of the main text, the corresponding local value of θ and hence $\nu_{dif,th} = \sin^2(\theta) - \cos^2(\theta)$ is obtained. Averaging over all positions in the lattice yields $\overline{n_p^2 U_p}$, $\overline{n_0 \Delta E}$, used in figure A.3(a) and $\overline{\nu}_{dif,th}$ plotted in figure 3 of the main text.

A.9. Measurement of $\langle\nu_{dif}\rangle$ and comparison to theory $\overline{\nu}_{dif,th}$

In order to obtain figures 3(a)–(f) of the main text, in equation (A.1) ϵ_y is adjusted to the six different values $1-\epsilon_y \in \{0.019, 0.014, 0.009, 0.004, 0.001, -0.001\}$ and β is varied for each setting. Momentum spectra are recorded and the number of atoms $n_\pm$ in the two zero order Bragg peaks corresponding to $X_\pm$ are counted. A data point in figures 3(a)–(f) represents an average over eight measurements. We thus obtain $\langle\nu_{dif}\rangle \equiv (\langle n_+\rangle - \langle n_-\rangle)/(\langle n_+\rangle + \langle n_-\rangle)$ for different combinations of the parameters β and ϵ_y. From β one obtains ΔV (see section A.1) and thus ν_p (see section A.6). The value ΔE is determined from a band calculation for the potential in equation (A.1) (see section A.7). For each data point, n_0 and $n_p = \nu_p n_0$ are derived at the time of the measurement, thus accounting for band relaxation loss. With this the energies $\overline{n_p^2\,U_p}$, $\overline{n_0\,\Delta E}$ and the occupation difference $\overline{\nu}_{dif,th}$ are obtained (see section A.8). The data points in each of the graphs (a)–(f) in figure 3 of the main text correspond to a path in the plane spanned by the energies $\overline{n_p^2\,U_p}$ and $\overline{n_0\,\Delta E}$. These paths are identified here in figure A.3(a). For the case of the red dashed path corresponding to figure 3(b), the local value of $\nu_{dif,th}$ is plotted across the lattice in figure A.3(b). This confirms that, particularly for the data points in the center of the path, finite size effects are in fact substantial and have to be accounted for.

A.10. Mean field predictions of $\overline{\nu}_{\mathrm{dif,th}}$ for real superposition state and incoherent mixture

We have also minimized the total energy for the real coherent superposition $\sin(\theta)\,|\psi_+\rangle \pm \cos(\theta)\,|\psi_-\rangle$ (scenario C) and for the incoherent mixture of spatially superimposed condensates $\sin^2(\theta)\,|\psi_+\rangle\langle\psi_+| + \cos^2(\theta)\,|\psi_-\rangle\langle\psi_-|$ (scenario D) in order to calculate the local mixing angle θ as a function of ΔE and ν_{p} and hence to determine $\nu_{\mathrm{dif,th}} = \sin^2(\theta) - \cos^2(\theta)$. For scenario C we obtain the simple result that $\nu_{\mathrm{dif,th}}$ is constrained to the values ± 1 depending on the sign of ΔE with no dependence upon ν_{p}. For scenario D, values of $\nu_{\mathrm{dif,th}}$ deviating from ± 1 require $\nu_{\mathrm{p}} > 2/3$ and satisfy

$$\nu_{\mathrm{dif,th}} = \frac{3\Delta E}{(\nu_{\mathrm{p}}^2 - 4\,(1-\nu_{\mathrm{p}})^2)\,n_0\,U_{\mathrm{p}}}\,. \tag{A.3}$$

An average over all plaquettes of the lattice as described in section A.8 leads to the corresponding value of $\overline{\nu}_{\mathrm{dif,th}}$, which yields the (blue) dashed traces in figure 3 of the main text.

References

[1] Tokura Y and Nagaosa N 2000 *Science* **288** 462–8
[2] Maeno Y, Hashimoto H, Yoshida K, Nishizaki S, Fujita T, Bednorz J G and Lichtenberg F 1994 *Nature* **372** 532–4
[3] Beenakker C W J 2013 *Annu. Rev. Condens. Matter Phys.* **4** 113–36
[4] Lewenstein M *et al* 2007 *Adv. Phys.* **56** 243–379
[5] Bloch I, Dalibard J and Zwerger W 2008 *Rev. Mod. Phys.* **80** 885–964
[6] Feynman R P 1972 *Statistical Mechanics, A Set of Lectures* (Boston, MA: Addison-Wesley)
[7] Wu C 2009 *Mod. Phys. Lett.* B **23** 1–24
[8] Lin Y-J, Compton R L, Jimnez-Garca K, Porto J V and Spielman I B 2009 *Nature* **462** 628–32
[9] Lin Y-J, Jimnez-Garca K, Porto J V and Spielman I B 2011 *Nature* **471** 83–6
[10] Dalibard J, Gerbier F, Juzeliūnas G and Öhberg P 2011 *Rev. Mod. Phys.* **83** 1523–43
[11] Aidelsburger M, Atala M, Nascimbéne S, Trotzky S, Chen Y-A and Bloch I 2011 *Phys. Rev. Lett.* **107** 255301
[12] Eckardt A, Weiss C and Holthaus M 2005 *Phys. Rev. Lett.* **95** 260404
[13] Zenesini A, Lignier H, Ciampini D, Morsch O and Arimondo E 2009 *Phys. Rev. Lett.* **102** 100403
[14] Struck J, Ölschläger C, Le Targat R, Soltan-Panahi P, Eckardt A, Lewenstein M, Windpassinger P and Sengstock K 2001 *Science* **333** 996–99
[15] Isacsson A and Girvin S 2005 *Phys. Rev.* A **72** 053604
[16] Liu W V and Wu C 2006 *Phys. Rev.* A **74** 013607
[17] Wirth G, Ölschläger M and Hemmerich A 2001 *Nature Phys.* **7** 147–53
[18] Hemmerich A, Schropp D and Hänsch T W 1991 *Phys. Rev.* A **44** 1910–21
[19] Ölschläger M, Wirth G and Hemmerich A 2011 *Phys. Rev. Lett.* **106** 015302
[20] Cai Z and Wu C 2011 *Phys. Rev.* A **84** 033635
[21] Liu B, Yu X-L and Liu W-M 2012 arXiv:1211.2595v3
[22] Cai Z, Duan L-M and Wu C 2012 *Phys. Rev.* A **86** 051601
[23] Sherson J F, Weitenberg C, Endres M, Cheneau M, Bloch I and Kuhr S 2010 *Nature* **467** 68–72
[24] Bakr W S, Peng A, Tai M E, Ma R, Simon J, Gillen J I, Fölling S, Pollet L and Greiner M 2010 *Science* **329** 547–50
[25] Li X, Zhao E and Liu W V 2011 *Phys. Rev.* A **83** 063626
[26] Pinheiro F, Martikainen J-P and Larson J 2012 *Phys. Rev.* A **85** 033638
[27] Martikainen J-P and Larson J 2012 *Phys. Rev.* A **86** 023611
[28] Ölschläger M, Wirth G, Kock T and Hemmerich A 2012 *Phys. Rev. Lett.* **108** 075302
[29] Sun K, Liu W V, Hemmerich A and Das Sarma S 2012 *Nature Phys.* **8** 67–70